Ion Acceleration at Magnetotail Plasma Jets

L. Richard[1,2], Yu. V. Khotyaintsev[1], D. B. Graham[1], A. Vaivads[3], R. Nikoukar[4], I. J. Cohen[4], D. L. Turner[4], S. A. Fuselier[5,6], C. T. Russell[7]

[1]Swedish Institute of Space Physics, Uppsala, Sweden
[2]Space and Plasma Physics, Department of Physics and Astronomy, Uppsala University, Sweden
[3]Space and Plasma Physics, School of Electrical Engineering, KTH Royal Institute of Technology, Stockholm, Sweden
[4]The Johns Hopkins University Applied Physics Laboratory, Laurel, Maryland, USA
[5]Southwest Research Institute, San Antonio, TX, USA
[6]Department of Physics and Astronomy, University of Texas at San Antonio, San Antonio, TX, USA
[7]Department of Earth Planetary and Space Sciences, University of California Los Angeles, Los Angeles, CA, USA

Key Points:

- Heavy ions of solar wind origin dominate fluxes at energies > 100 keV due to charge-state-dependent energization.
- Ions with gyroradii smaller than the scale of the structure ($\rho_p < L_y$) gain energy from the ion bulk flow.
- Ions with gyroradii $\rho_p \gtrsim L_y$ gain energy from non-adiabatic interaction with the electric field pulse.

Corresponding author: Louis Richard, louis.richard@irfu.se

Abstract
We investigate a series of Earthward bursty bulk flows (BBFs) observed by the Magnetospheric Multiscale (MMS) spacecraft in Earth's magnetotail at (-24, 7, 4) R_E in Geocentric Solar Magnetospheric (GSM) coordinates. At the leading edges of the BBFs, we observe complex magnetic field structures. In particular, we focus on one which presents a chain of small scale ($\sim 0.5\ R_E$) dipolarizations, and another with a large scale ($\sim 3.5\ R_E$) dipolarization. Although the two structures have different scales, both of these structures are associated with flux increases of supra-thermal ions with energies $\gtrsim 100$ keV. We investigate the ion acceleration mechanism and its dependence on the mass and charge state. We show that the ions with gyroradii smaller than the scale of the structure are accelerated by the ion bulk flow. We show that whereas in the small scale structure, ions with gyroradii comparable with the scale of the structure undergo resonance acceleration, and the acceleration in the larger scale structure is more likely due to a spatially limited electric field.

1 Introduction

Plasma jets are ubiquitous phenomena in the universe (Phan et al., 2000; Masuda et al., 1994; Pudritz et al., 2012). In particular, in Earth's magnetotail, jets take the form of high speed ($V > 400$ km s^{-1}) transient Earthward plasma flows referred to as bursty bulk flows (BBFs) (Angelopoulos et al., 1992, 1994). These BBFs play a crucial role in magnetotail activity (Sitnov et al., 2019). BBFs are seen as short living narrow flow channels which last 10-100 s (Baumjohann et al., 1990) and extend over $\sim 1 - 5\ R_E$ in the dawn-dusk direction (Nakamura et al., 2004). At the leading edge, BBFs are accompanied by a sharp dipolarization (i.e., increase of the northward magnetic field B_z) of the magnetic field called dipolarization fronts (DFs) (Nakamura et al., 2002; Ohtani, 2004; Runov et al., 2009; Sergeev et al., 2009).

DFs are thin ion-scale boundaries similar to vertical current sheets (Runov et al., 2011; Liu et al., 2013), which separate the lower temperature dense plasma ahead of the DF from the hotter tenuous plasma behind the DF (Khotyaintsev et al., 2011; Fu et al., 2013). Various mechanisms are thought to be responsible for the formation of DFs, such as the ballooning/interchange instability (Pritchett & Coroniti, 2010) and unsteady magnetic reconnection (Sitnov et al., 2009; Fu et al., 2013).

Electron acceleration associated with DFs has been widely observed using Cluster (Apatenkov et al., 2007), THEMIS (Runov et al., 2009) and MMS (Turner et al., 2016). The two main mechanisms responsible for the acceleration of electrons are the betatron acceleration due to Earthward transport of electrons in the increasing magnetic field (Birn et al., 2013) and Fermi acceleration due to shrinking of the magnetic field lines during the Earthward convection (Fu et al., 2011). In particular, Fu et al. (2011) showed that betatron acceleration dominates in the growing flux pileup region, while Fermi acceleration dominates in the decaying flux pileup region. On the other hand, Malykhin et al. (2018) showed that changes in the spectral index of electrons is sometimes associated with high-frequency waves. Malykhin et al. (2018) suggested that the spectral index changes are due to non-adiabatic wave-particle interaction, which results in electron acceleration and/or scattering.

Ion acceleration at DFs has been extensively studied by means of numerical simulations and observations (Fu et al., 2020). In particular, test particle simulations in assumed or simulated electromagnetic field pulses carried out by Birn and Hesse (1994) and Birn et al. (1997, 2000, 2013, 2015, 2017), showed that the ions get accelerated by the motional cross-tail electric field, while gyrating inside the $\mathbf{E} \times \mathbf{B}$ Earthward-convecting structure. Since the magnetic field increased during the Earthward convection, they concluded that the ions undergo a quasi-adiabatic betatron-like acceleration. On the other hand, observations and the particle simulation by Zhou et al. (2010, 2011), showed the formation of an energized ion population ahead of the DF due to ion reflection from the DF similar to that at shocks (Gosling et al., 1982). Zhou et al. (2011) showed that in the presence of a finite northward

magnetic field, the energized population is confined to an ion-scale region ahead of the DF. Similarly, Ukhorskiy et al. (2013) showed that the negative magnetic dip observed in the soliton-like magnetic field structure (Runov et al., 2009) is bounded by two magnetic null points, which are local maximum and minimum of the effective potential energy, and hence creates a potential well. The potential well leads to trapping of the ions between the DF (local potential maximum) and the reconnection point (local potential minimum) ahead of the DF. Recently, Ukhorskiy et al. (2017, 2018) showed that ions can be stably trapped in the inverse magnetic field gradient and gain energy through persistent interactions with the motional electric field.

Moreover, Ukhorskiy et al. (2017, 2018) showed that the acceleration enabled by stable trapping in the inverse magnetic field gradient is charge-state-dependent and mass independent. Similarly, the test particle simulation of ion acceleration in stochastic electromagnetic perturbations carried out by Catapano et al. (2017), showed that the energization is linearly dependent on the charge state, while only weakly mass dependant. Mitchell et al. (2018) showed using the Van Allen Probes at $5 < L < 7$ and a simple model of Earthward flow limited in azimuthal extent, that the energization is adiabatic or quasi-adiabatic and therefore, the particle trajectories and energization depends only on ion charge state and not on the ion mass. Using, the Energetic Ion Spectrometer (EIS) on the Magnetospheric Multiscale (MMS) spacecraft, Bingham et al. (2020) found a case of ion energization in the magnetotail ordered by charge state.

Nevertheless, due to their larger gyroradii, ion acceleration is much more complicated than electron acceleration, so that, detailed observations of ion acceleration at DFs are still lacking with respect to those of electron acceleration. In particular, the identification of the different acceleration mechanisms acting at scales smaller than, comparable to, and larger than the scale of the magnetic field structures and the adiabaticity of the acceleration mechanism at the aforementioned scales are still open questions. Here, we investigate the ion acceleration at turbulent reconnection jet fronts in order to advance our understanding of these questions.

2 Observations

We use the magnetic field measurements from the Fluxgate Magnetometer (FGM) (Russell et al., 2016), the electric field measurements from the Electric field Double Probe (EDP) (Ergun et al., 2016; Lindqvist et al., 2016), and the ion and electron distributions and their moments from the Fast Plasma Investigation (FPI) (Pollock et al., 2016), the Hot Plasma Composition Analyser (HPCA) (Young et al., 2016), the Fly Eye Energetic Particle Spectrometer (FEEPS) (Blake et al., 2016) and the Energetic Ion Spectrometer (EIS) (Mauk et al., 2016). The FPI instrument measures the ion and electron distributions in the thermal energy range $K \in [0.01 - 30$ keV$]$ assuming that the ion flux is fully dominated by the protons. We note that due to penetrating radiation effects, we correct the FPI-DIS moments according to the procedure described in Gershman et al. (2019). The HPCA instrument measures the ion flux over a broader energy range $K/q \in [0.01 - 40$ keV$/q]$ with a mass resolution $m/q \in [1 - 16$ a.m.u$/e]$ (i.e., H^+, He^+, He^{2+} and O^+) using a carbon-foil based time-of-flight analyser. The FEEPS instrument measures ions, with no mass resolution, and electron flux in the energy ranges $K_i \in [40-1000$ keV$]$ and $K_e \in [20-1000$ keV$]$, respectively. The EIS instrument measures ion flux in the energy range $K/q \in [20-1000$ keV$]$ with time-of-flight based mass resolution (H^+, He^{n+}, and O^{n+}). For all instruments, we used both Fast Survey and Burst data.

We investigate a series of bursty bulk flows (BBFs) observed by the Magnetospheric Multiscale (MMS) spacecraft on July 23rd, 2017 between 16:10:00 UT and 18:10:00 UT. For this time period, the spacecraft were located in the magnetotail at (-24, 7, 4) R_E in Geocentric Solar Magnetospheric (GSM) coordinates, where R_E is Earth's radius, as shown in Figure 1a and 1b. The black lines in Figure 1b show Earth's magnetic field lines computed

using the T89 model (Tsyganenko, 1989). During the time interval of the observations, the substorm activity was moderate with the AE index reaching ~ 400 nT.

During the event, the spacecraft separation shown in Figure 1c, was $\Delta R \sim 10$ km $\sim 0.01 d_i$, where the ion inertial length $d_i = 740$ km is the typical thickness of a DF (Runov et al., 2009). As we are interested in energetic ions, which have the gyroradius much larger than the spacecraft separation scale, the fields measurements from FGM and EDP, and the ion moments from FPI-DIS are computed at the center of mass of the tetrahedron formed by the MMS spacecraft. Taking advantage of the small spacecraft separation, the FEEPS instruments onboard all spacecraft are combined together to provide a larger instantaneous field of view and better counting statistics. The same method was applied to EIS. Because of small discrepancies between the spacecraft, data from HPCA were taken from the MMS 2 spacecraft which offers the best agreement with other instruments.

2.1 Overview

An overview of the event is shown in Figure 1. Initially, the magnetic field (Figure 1d) is predominantly tailward (large negative B_x) which indicates that the MMS spacecraft were located southward of the magnetotail neutral sheet. Using the plasma moments from FPI, we plot in Figure 1i, the plasma beta $\beta = p/p_{mag}$ with p the plasma pressure and $p_{mag} = |\mathbf{B}|^2/2\mu_0$ the magnetic pressure. Using the criteria by Haaland et al. (2010) to classify the regions, we observe that, consistent with the T89 model shown in Figure 1b, the MMS spacecraft were initially in the plasma sheet boundary layer (PSBL, $0.01 < \beta < 0.2$) and then went into the central plasma sheet (CPS, $\beta > 0.7$). We note two excursions into the lobe ($\beta < 0.01$) at 16:25:00 UT and 16:40:00 UT, suggesting a global north-south motion of the plasma sheet. Furthermore, we see that the Earthward magnetic field B_x observed in the lobe at 16:40:00 UT is weaker than the one initially observed in the PSBL ~ 20 nT at 16:10:00 UT, which suggests a possible thinning/stretching of the plasma sheet possibly related to the growth phase of the substorm.

The MMS spacecraft observed a quasi-steady Earthward jet with $V_x \sim 1000$ km s^{-1} lasting until 16:40:00 UT, which is followed by 5 Earthward BBFs (Figure 1f). In particular, we note that the last BBF at 17:20:00 UT, exhibits oscillations of the Earthward ion bulk velocity with a period of ~ 2 min. Similar observations of BBF oscillations have been reported by Panov et al. (2010) using the THEMIS spacecraft and by Merkin et al. (2019) using the Lyon-Fedder-Mobarry (LFM) model run. Merkin et al. (2019) concluded that these oscillations are a signature of a BBF overshooting its equilibrium and oscillating until settling in (Chen & Wolf, 1999). At the leading edge of the BBFs, we observe in the FEEPS omni-directional ion and electron energy spectra plotted in Figures 1k and 1m respectively, strong sharp energization of the thermal ions and electrons. Associated with the energization of the thermal particles, we observe a flux increase of the supra-thermal ions and electrons in Figures 1j and 1l respectively. We note that energetic ions and electrons are also seen outside of the BBFs but since the BBFs are the primary subject of the paper, we focus on those observed at the leading edge of the Earthward flows. We marked the BBF-associated peaks in the energetic ion flux by the dashed black lines. The peaks are associated with large drops in the ion density (Figure 1g), increases in the ion temperature (Figure 1h), and dipolarizations (increased B_z) of the magnetic field (Figure 1d), which are followed by large amplitude electric field activity (Figure 1e). Based on these properties we identify these structures as DFs.

In order to focus the study of ion energization processes, we select intervals based on the supra-thermal ion flux at 200 keV. Using the FEEPS omni-directional ion energy spectrum, which does not separate between the different ion masses, we identify the energization times as:

$$J^{200} > 2\sigma_{J^{200}} = 2\sqrt{\frac{\sum_{i=1}^{n}\left(J_i^{200} - \bar{J}^{200}\right)}{N-1}} \quad (1)$$

where J^{200} is the ion flux at 200 keV, $\bar{J}^{200}$ its mean value over the 2 hours interval 16:10:00 - 18:10:00 UT and N the number of time records. The condition defined by Equation 1 corresponds statistically to a 95th percentile threshold in a normal distribution. The marked times at the top of Figure 1d, reveals three clusters with two that are associated with a high speed $V_x > 500$ km s^{-1} jet. Since the third cluster is not associated with a BBF, we focus only on the two first intervals henceforth refered to as event I (16:54:14-16:59:26 UT) and event II (17:17:04-17:22:36 UT). These two intervals are indicated by purple shading in Figures 1d to 1m. In the rest of the paper, we focus on the ion acceleration during these two intervals.

2.2 Ion Composition and Charge-State-Dependent Acceleration

In order to characterize the ion acceleration, it is important to know the composition of the supra-thermal ions. We plot in Figure 2d the time series of the Fast Survey Mode proton flux at different energies. At low (thermal) energies $K_p < 40$ keV, we use the proton H^+ flux from the HPCA instrument. At higher energies $K_p > 20$ keV we use the proton H^+ flux from the EIS instrument. We also plot in Figure 2e the Fast Survey Mode Helium flux. At low energies ($K_{He^{n+}} < 80$ keV) we use the He^{2+} flux from HPCA, which offers both mass and charge state resolution. At supra-thermal energies, we use the He^{n+} flux from the EIS instrument which, unlike HPCA, does not provide charge state resolution. We note that, although HPCA also provides the He^+ flux, for this event no significant He^+ flux was observed at energies < 40 keV. The O^{n+} ions also measured by the EIS instrument are not treated in this study due to low statistics (i.e. large errors $\delta f/f = 1/\sqrt{n}$, with n the number of counts assuming that the counting statistics are described by Poisson's statistics) in the EIS energy range. Finally, we plot in Figure 2f the Fast Survey Mode electron flux, where the low energies ($K_e < 30$ keV) are measured by the FPI-DES instrument while energies $K_e > 30$ keV are measured by the FEEPS instrument.

At energies $K < 10$ keV, the electron flux (Figure 2d) dominates the ion (proton and heavy ions) flux (Figure 2e). Similar intensity dominance of < 10 keV electrons, have been observed by Runov et al. (2015) using the THEMIS spacecraft. At energies 10 keV $< K <$ 150 keV, the flux is dominated by the proton flux, while at higher energies $K > 150$ keV the flux is dominated by the helium flux. This result is consistent with observation at $6 < L < 16.5$ by Cohen et al. (2017), who showed the intensity dominance for $K > 150$ keV of multiply-charged heavy ions in the magnetosphere.

In order to identify the charge state of the observed He^{n+} ions from EIS measurement, we use the correlation technique introduced by Mitchell et al. (2018) for Van Allen Probes RBSPICE measurements, and later employed for MMS EIS measurements by Bingham et al. (2020, 2021). From the bounce-averaged guiding center description of particle motion (Kistler et al., 1989),

$$\frac{\mathrm{d}\mathbf{x}}{\mathrm{dt}} = \mathbf{v}_{\mathbf{E}\times\mathbf{B}} + \frac{K_\perp}{qB}\frac{\mathbf{B}\times\nabla\mathbf{B}}{\mathbf{B}^2} + \frac{2K_\parallel}{qB}\frac{\mathbf{R_c}\times\mathbf{B}}{{\mathbf{R_c}}^2 B} \quad (2)$$

where $\mathbf{x}$ is the position of the guiding center, $\mathbf{v}_{\mathbf{E}\times\mathbf{B}} = \mathbf{E}\times\mathbf{B}/|\mathbf{B}^2|$ is the drift velocity and $\mathbf{R_c}$ is the radius of curvature of the magnetic field, it follows that the ions with the same K/q follow the same trajectories and are energized in a charge-state-dependant manner. Due to the charge state dependence of the second and third terms of Equation 2, Schulz and Lanzerotti (1974) showed that the temporal flux changes are ordered by K/q. Using this result, Mitchell et al. (2018), used the correlation of the temporal changes of the Van Allen Probes RBSPICE measurements of the proton and heavy ion fluxes to infer the charge state of the heavy ions. A large cross-correlation coefficient between the proton flux at the energy

K_{H^+} and the flux of the specie s at the energy $K_s = q_s K_{H^+}$, would suggest that the most likely charge state of the species s is q_s.

On large scales, we observe that the flux changes of the protons (Figure 2d) and the Helium ions (Figure 2e) are qualitatively well correlated. We note that every injection (supra-thermal ions flux increase at the DFs) marked by the black dashed lines is dispersionless (i.e., the flux increase occurs at the same time at all energies). In Figure 3 we plot the cross-correlation coefficient between the changes in the Burst mode H^+ and He^{n+} fluxes during the time interval 16:10:00 - 18:10:00 UT. The total length of the Burst data is about 1 hour ($\sim$ 180 omni-directional spin-averaged points) with some gaps. In order to guide the eye, we mark with yellow boxes the energies that satisfy the relation $K_{He^{n+}} = q * K_{H^+}$ where $q = 1$ corresponds to He^+ and $q = 2$ to He^{2+}. We observe a ridge of high correlation which falls within the yellow boxes corresponding to $q = 2$, indicating that on large scales the dynamics is ordered by K/q, and that the dominant charge state of the helium is likely He^{2+}, consistent with the aforementioned observation of He^{2+} and no He^+ at thermal energies ($K/q < 40$ keV/q). This result indicates that during our event in the magnetotail, the heavy ions are of solar wind origin, consistent with the MMS observations by Bingham et al. (2020, 2021).

To investigate whether the dynamics are ordered by K/q on local scales, we compare the flux enhancement for H^+ and He^{n+} as a function of the energy per charge K/q for the two selected intervals. To do so, we assume that the source population is upstream of the DF. Indeed, as shown in the combined MHD/test particle simulations by Birn et al. (2013, 2015), the main source of accelerated ions is the central plasma sheet. Furthermore, we can assume that the plasma sheet is rather homogeneous in the dawn-dusk direction on the scale of the flow channel ($1 - 5\ R_E$). Hence, we assume that the source population is the plasma sheet at rest far ahead of the acceleration site (i.e., the DF). We emphasize the importance of using a source region far from the DF, at least a few ion gyroradii, because of possible contamination by the DF-reflected ions ahead of the DF (Zhou et al., 2010, 2011). On the other hand, the energized distribution is taken at the time of peak of the proton flux at $K_p \approx 70$ keV.

For event I (16:54:14-16:59:26 UT), we observe that the magnetic field is highly variable with a chain of small scale structures in Figure 4a. The characteristic time scale of the magnetic field structures is $\tau = 5$ s. Using the average ion bulk velocity associated with the magnetic field structures $V_i = 830 \pm 110$ km s^{-1}, a characteristic spatial scale of $L_x = 0.65 \pm 0.08\ R_E$ is calculated in the Earth-tail direction. We plot the EIS proton (blue) and combined HPCA/EIS helium (red) omni-directional energy spectra in Figure 4b and 4c respectively. The time interval where we take the source and energized ion distributions are marked as "s." and "e.". We plot in Figure 4d and 4e the source (dashed lines) and energized (solid lines) enhancement omni-directional flux as a function of the ion energy K and ion energy per charge K/q, respectively, and the ratio of the energized to source fluxes in Figures 4f and 4g. As already mentioned, at energies > 150 keV the helium flux dominates the proton flux (Figure 4d).

The spectral slope of the flux as a function of the energy per charge plotted in Figure 4e, differs significantly between the species. In particular, at energies > 50 KeV/q, the Helium (He^{2+}) spectrum is harder (i.e., has a smaller spectral slope $|\gamma_s| = 3.7,\ |\gamma_e| = 2.6$), than that of the protons ($|\gamma_s| = 4.6,\ |\gamma_e| = 4.8$). To compute the energy per charge ratio, we assumed that the helium is in the alpha charge state He^{2+}, based on the above charge state analysis. When plotted as a function of the energy K, we observe that the flux ratio of the He^{2+} agrees with the one of the protons (Figure 4f). On the other hand, when plotted as a function of the energy per charge K/q, we observe that the flux ratio of the He^{2+} ions does not agree with the one of the protons (Figure 4g). This results indicates that at constant K/q, the flux changes of the He^{2+} ions differs from those of the protons, and thus the flux changes are not ordered by K/q, meaning that the energization does not depend solely on the ion charge state.

For event II (17:17:04-17:22:36 UT), the magnetic field (Figure 5a) in the wake of the DF has a stable configuration suggesting a large-scale structure with a spatial scale of $\sim 6\ R_E$ in the Earth-tail direction. The spectral slopes of the H^+ and He^{2+} ions are similar for both source and energized ions (Figure 5e). Such alignment of the spectral shape of different species have been observed using MMS by Bingham et al. (2020). Moreover, the flux ratio of the two species shows a very good agreement when plotted as a function of K/q in Figure 5g. This indicates that the energization likely depends solely on the charge state, which suggests direct acceleration of ions by the inductive electric field which is mass independent.

2.3 Acceleration of Protons

We now investigate the acceleration mechanisms responsible for the energetic ion enhancement for both intervals. Here, we focus on the proton acceleration mechanism since as shown in Figures 4 and 5, the larger statistics i.e., smaller errors are measured for protons. We plot in Figure 6d the source (orange) and energized (green) omni-directional proton phase space density energy spectra in the spacecraft frame. The phase space density f is computed from the proton flux measured by EIS using the standard relation between differential flux and phase space density (non-relativistic case)

$$f = \frac{m_p^2}{2K} J, \tag{3}$$

where m_p is the proton mass and K is the effective energy of the EIS energy channel. We observe that the two spectra are nearly parallel with some minor discrepancies.

To account for the effect of the bulk motion of the ion jet, we transform the proton velocity distribution into the proton bulk frame. To do so, we interpolate the proton distribution defined on the 3D spherical velocity space grid onto the same grid translated along the proton bulk velocity. Figure 6e shows the omni-directional phase space density energy spectra in the reference frame of the proton bulk flow. We observe good agreement between the source and energized distributions at energies < 50 keV, which suggests that the energization of the low energy protons is due to the bulk flow.

The energy gain δK at the same PSD level highlighted by the cyan-shaded region in Figure 6d and the purple-shaded region in Figure 6e are plotted in Figure 6f (cyan and purple squares) as a function of the initial energy K_0. We observe that the energy gain δK oscillates as a function of the initial energy K_0 ($\sigma_{\delta K}/\langle \delta K \rangle = 0.91$). In particular, at energies < 50 keV, $\delta K = 6.8 \pm 4.8$ keV which corresponds to $V_i = 1139 \pm 407$ km s^{-1}, consistent (within 0.74σ) with the average proton bulk speed $V_i = 830 \pm 110$ km s^{-1} observed in Figure 6c.

In the proton bulk frame for energies > 50 keV we observe a significant energy gain in Figure 6f. In particular, we observe a peak of the energy gain δK in the proton bulk frame (purple squares) at $K_0 \sim 140$ keV in Figure 6f. However, the large errors in the proton phase-space densities f at energies $K_0 > 140$ keV yield large uncertainties on the energy gain δK, so that it is difficult to conclude if the energy gain at $K_0 \sim 140$ keV is a real physical enhancement. On the other hand, we observe a bulge in the energy gain at $K_0 = 66.6 \pm 7.3$ keV in Figure 6f. We estimate the characteristic time scale $\tau = 5$ s $\approx 0.68\ f_{cp}^{-1}$ of the magnetic field structures (Figure 6b). Using the average ion bulk velocity associated with the magnetic field structure, it yields a spatial scale of $L_x = 0.65 \pm 0.08\ R_E$. The energy of a proton with a gyroradius so that $\rho_p = L_x$ is $K_p = 74.7 \pm 19.7$ keV (gold line), consistent with the energy $K_0 = 66.6 \pm 7.3$ keV of the bulge of energy gain.

Figure 7 shows data for the event II (17:17:04-17:22:36 UT) in the same format as Figure 6. We observe in Figure 7d that at energies < 50 keV, the energy gain δK in the spacecraft frame is rather constant and does not depend on the initial energy K_0. This

result is also seen in Figure 7f, where we observe a constant energization $\delta K = 8.4 \pm 1.9$ keV (cyan squares) at energies $K_0 < 50$ keV. This constant energization corresponds to $V_i = 1268 \pm 143$ km s^{-1}, which is consistent (within 1.95σ) with the 20 s (17:19:20-17:19:40 UT) average of the ion bulk speed $V_i = 732 \pm 235$ km s^{-1}, and comparable to the maximum ion bulk speed $V_i^{max} = 1001$ km s^{-1}.

To account for the effect of the bulk flow, we transform the proton distribution into the proton bulk frame using the 20 s (17:19:20-17:19:40 UT) average bulk velocity and plot the omni-directional phase space density energy spectrum in Figure 7e. We observe good agreement between the source (orange) and the energized (green) spectra at low energies < 50 keV, and a negligible energy gain δK in the proton bulk frame shown in Figure 7f. This result suggests that, similar to the event I (16:54:14-16:57:25 UT), the energization of the low energy proton < 50 keV is due to the proton bulk flow.

On the other hand, for protons with initial energy > 50 keV (i.e., $\rho_p > 0.52\ R_E$), we observe a significant energy gain in the proton bulk frame in Figures 7e and 7f, which suggests that protons with a gyroradius $\rho_p < 0.52\ R_E$ have a zero net energy gain in the proton bulk frame, while protons with a gyroradius $\rho_p > 0.52\ R_E$ gain energy. This net energy gain suggests that, for protons with a gyroradius $\rho_p < 0.52\ R_E$ the energy gained from the cross-tail electric field during the duskward part of the gyration is compensated by the energy loss during the dawnward part of the gyration. On the other hand, for a proton with a gyroradius $\rho_p \gtrsim 0.52\ R_E$ part of the decelerating dawnward part of the proton gyration is outside of the electric field region, and thus does not compensate the energization during the duskward part of the orbit. Preferential acceleration of protons with $\rho_p \gtrsim 0.52\ R_E$ indicates that the electric field structure, which is the acceleration region, is spatially limited. In Figure 7f we plot (black dashed line) the model proposed by Artemyev et al. (2015), of the acceleration of protons in a spatially limited electric field pulse $\delta K = 2eE_y\rho_p \propto \sqrt{K_0}$. We observe that at energies $K_0 > 100$ keV, the model agrees with the measured energy gain, but at energies 50 keV $< K_0 < 100$ keV, because the proton orbit in the acceleration region is much more complicated than a simple half gyration described by Artemyev et al. (2015), the model overestimates the energy gain.

3 Discussion

We found that for both the small-scale turbulent and the large-scale magnetic field structures, at energies < 50 keV the proton energization is of the order of the proton bulk energy $\delta K \sim K_{bulk}$ in the spacecraft frame, so that $\delta K \sim 0$ in the proton frame. This suggests that protons with energies < 50 keV gyrate inside the $E \times B$ earthward convected magnetic field structure with no net energy gain. In this scenario, the energy gain due to the interaction with the cross-tail motional electric field during the first half (duskward) of the gyration, is suppressed during the second half (dawnward) where the particle is slowed down by the same electric field. So that, over one gyration no net energy is gained by the ion. Hence, we conclude that ions with a gyroradius $\rho_p < L_y$ with L_y is the dawn-dusk scale of the structure, are $E \times B$ drifting without gaining energy from the interaction with the electric field.

In the event I (16:54:14-16:57:25 UT), we found that the ion flux changes associated with the acceleration are not ordered by K/q, which implies that the energization is non-adiabatic. Indeed, the ion motion is adiabatic when the scales (both temporal τ and spatial $L_x,\ L_y$) of the electromagnetic fluctuations are larger than the ion scales (gyroperiod f_{cp}^{-1} and gyroradius ρ_p). In such case Equation 2 implies that the energization is ordered by K/q. For the event I, we observe that the flux changes are not ordered by K/q. Hence, the energization process does not depend solely on the charge state, which implies that the energization is non-adiabatic.

The later result is also supported by our observation of electromagnetic fluctuations on temporal scales comparable to the ion gyroperiod, which contributes to the violation of the first adiabatic invariant. In the event I (16:54:14-16:57:25 UT), we observe that only the ions with gyroradius of $\rho_p \sim L_x$, where L_x is the Earth-tail scale of the electromagnetic field structure, experience significant energization. This preferential energization suggests that the electromagnetic energy injected in the form of large scale structures (BBF) cascades down to the ion scales where it dissipates in the form of particle acceleration. Using Cluster, Malykhin et al. (2018) observed a similar bulge in the proton energy spectrum in the 70 keV − 90 keV energy range. They explained the formation of such bulge by the non-adiabatic resonant interaction of thermal protons with the DFs (Artemyev et al., 2012). Using the analytical model of non-adiabatic resonant interaction proposed by Artemyev et al. (2012), we can estimate the dawn-dusk scale of the DF as $L_y = W/|qE_y|$. We estimate the dawn-dusk scale of the DF to be $L_y = 1.02 \pm 0.11 R_E$, consistent with the typical dawn-dusk scales of the BBFs in the magnetotail (Nakamura et al., 2004). This prediction, and the underlying model, are valid under the assumption that the acceleration time must be shorter than the time scale of the magnetic fluctuation or $L_x > L_{x0} = \sqrt{L_y v_\phi / \pi f_{cp}}$, where v_ϕ is the DF velocity assumed to be equal to the bulk velocity and L_x is the spatial scale of the magnetic field fluctuations. It follows that the condition is satisfied $L_x = 0.65 \pm 0.08\ R_E > L_{x0} = 0.52 \pm 0.03\ R_E$. Hence, we conclude that the ions energization is due to the resonant interaction of the $\sim$ 70 keV ions with the inductive electric field associated with the DF.

For the event II (17:17:04-17:22:36 UT), we found that the ion flux changes are well ordered by K/q. We note that the charge-state-dependent energization is a necessary condition but it does not necessarily imply adiabaticity of the energization process (Catapano et al., 2017; Ukhorskiy et al., 2018). We observed that at energies above the threshold energy of 50 keV (i.e., $\rho_p \gtrsim 0.52\ R_E$), the energization depends on the initial proton energy. Preferential acceleration of protons with $\rho_p \gtrsim 0.52\ R_E$ indicates that the electric field structure (i.e., the acceleration region) is spatially limited. Since the accelerating force is the cross tail motional electric field, the characteristic acceleration scale is thus the dawn-dusk scale L_y of the BBF. The energy dependence of the acceleration above 50 keV suggests that the characteristic dawn-dusk scale is comparable to the gyroradius at this threshold energy $\sim 0.52\ R_E$. We conclude that the dawn-dusk scale of the acceleration region is $\sim 0.52\ R_E$. This is much smaller than the typical scale of the flow channel $2 - 3\ R_E$ (Nakamura et al., 2004).

Using the model of the spatially limited electric field structure proposed by Artemyev et al. (2015), we showed that at energies $\sim$ 100 keV the model agrees with our observation while for lower energies, the observed energy gain is lower than the predicted one. This overestimation of the energy gain by the model is likely due to simplified proton orbits in the model proposed by Artemyev et al. (2015). Indeed, in the model of spatially limited electric field pulse, the ion is assumed to interact with the dawn-dusk electric field during its complete duskward half gyration. However, this scenario is valid if the ion interacts with the electric field pulse during the duskward half gyration only, and that the dawn-dusk scale of the acceleration region is larger than the ion gyroradius. In particular, this model does not take into account the case of interaction of the ion with the electric field pulse during the dawnward gyration which leads to deceleration of the ion, or the case of an ion which leaves the acceleration before the completing the dawnward half gyration.

Furthermore, we observed that the energy gained by protons with initial energy 50 keV $< K_p <$ 100 keV, represents a significant fraction of the initial energy up to $\sim$ 50 %. This result indicates that protons with gyroradius comparable to the dawn-dusk scale L_y of the acceleration region (i.e., dawn-dusk scale of the BBF), gain energy from the motional electric field in a non-adiabatic manner. On the other hand, as mentioned by (Artemyev et al., 2015), for protons with gyroradius $\rho_p \gg L_y$ of the electric field structure, the approximation $L_y \sim 2\rho_p$ used in the model is no longer valid, so that the energy increase becomes

$\delta K = eE_y L_y$. This means that the energy gain does not depend on the initial energy, and hence $\delta K/K_0 \propto 1/K_0$ or $\delta\rho_i/\rho_{i0} \propto 1/\sqrt{K_0}$. For protons with high initial energy, the energy gain during interaction with individual electric pulses, represents only a small fraction of their initial energy, thus their behavior is close to adiabatic. Hence, we conclude that protons with gyroradius comparable with the dawn-dusk scale of the electric field pulse $\rho_p \sim L_y$ are non-adiabatically accelerated, whereas protons with gyroradius much larger $\rho_p >> L_y$ are accelerated in an adiabatic manner.

We showed that the energization occurs for protons with gyroradius comparable with the scale of the acceleration region. So that, $L \sim \rho_i = \sqrt{\alpha}\rho_{H^+}/q$, where $\alpha = m_i/m_p$, and the corresponding ion energy $K_0 = q^2 K_{0,H^+}/\alpha$. In particular, for He^{2+} $\alpha = 4$ and $q = 2$, which yields that H^+ and He^{2+} ions with equal energies $K_{0,He^{2+}} = K_{0,H^+}$ have equal gyroradii. However, we showed that, especially for the event II (17:17:04-17:22:36 UT), the flux changes are well ordered by K/q similar to that found in Catapano et al. (2017) and Ukhorskiy et al. (2018). This result suggests that the acceleration of heavier ions occurs at scales larger than that for protons. On the other hand, preferential acceleration of heavier ions ($m_i/m_p > 1$) may results from interaction with electromagnetic fluctuations with time scales on the heavier ion gyro-periods (Keika et al., 2013). In such a scenario, the protons with gyroradius smaller than the scale of the structure have a zero net energy gain. At the same time, heavier ions with gyroradius smaller than the scale of the structure but gyroperiod on the time scale of the fluctuations are accelerated through interaction with the inductive electric field.

To summarize, we showed that in both cases the acceleration is due to Earthward moving electric field pulses. The protons with gyroradius smaller than the dawn-dusk scale of the electric field pulse have no net energy gain due to compensation of the energy gain during the duskward half of the gyration by the energy loss during the dawnward half of the gyration. We showed that when the temporal scale of the electromagnetic fluctuations is much larger than the proton gyroperiod (second time interval), protons with gyroradius larger than the scale of the electric field pulse gain energy through crossing of the electric field pulse. On the other hand, when the temporal scale of the electromagnetic fluctuations is of the order of the proton gyroperiod (first time interval) trapped protons with gyroradius of the order of the scale of the electric field pulse gain energy through resonant interaction with the inductive electric field. We note that the non-adiabatic acceleration by spatially limited electric field pulses is much more efficient than the non-adiabatic acceleration by resonant interaction with the inductive electric field.

4 Conclusion

We have presented observations of ion acceleration related to plasma jets (bursty bulk flows) in the Earth's magnetotail during a moderate substorm activity. We observed that the > 100 keV ions consist primarily of solar wind Helium He^{2+}, while the < 100 keV ion flux is dominated by the protons.

We study in detail two jets fronts with different characteristics. We find that in the event I (16:54:14-16:57:25 UT) with a chain of small-scale magnetic field structures, protons with gyroradius comparable to the scale of the structure gain energy through resonant acceleration (Artemyev et al., 2012). We showed that the interaction of the protons with electromagnetic fluctuations on proton scales leads to a gain of energy in a non-adiabatic manner.

For the event II (17:17:04-17:22:36 UT) with a larger scale magnetic field structure, the protons with a gyroradius larger than scale of the structure, gain energy via interaction with the cross-tail motional electric field during the duskward part of their orbit. We find that the energy gain for protons with gyroradius of the order of the scale of the structure is proportional to their gyroradius and represent a significant fraction of their initial energy.

In both cases the energization occurs for protons with gyroradii of the order of the scale of the structure or larger. Protons with smaller gyroradii have no net energy gain from the electric field, so that their energy gain in the spacecraft frame is due the earthward convection of the magnetic structure.

Acknowledgments
We thank the entire MMS team and instrument PIs for data access and support. All data used in this paper are publicly available from the MMS Science Data Center `https://lasp.colorado.edu/mms/sdc/`. We also wish to thank A. Lalti and the International Space Science Institute (ISSI) working group on "Magnetotail Dipolarizations: Archimedes Force or Ideal Collapse?" for valuable discussions. Data analysis was performed using the pyrfu analysis package available at `https://pypi.org/project/pyrfu/`. The codes to reproduce the figures in this paper are available at `https://github.com/louis-richard/ionacc` and additional data are available at `https://doi.org/10.5281/zenodo.6320624`. This work is supported by the Swedish National Space Agency grant 139/18.

References

Angelopoulos, V., Baumjohann, W., Kennel, C. F., Coroniti, F. V., Kivelson, M. G., Pellat, R., ... Paschmann, G. (1992). Bursty bulk flows in the inner central plasma sheet. *Journal of Geophysical Research*, *97*(A4), 4027–4039. doi: 10.1029/91JA02701

Angelopoulos, V., Kennel, C. F., Coroniti, F. V., Pellat, R., Kivelson, M. G., Walker, R. J., ... Gosling, J. T. (1994). Statistical characteristics of bursty bulk flow events. *Journal of Geophysical Research*, *99*(A11), 21257–21280. doi: 10.1029/94JA01263

Apatenkov, S. V., Sergeev, V. A., Kubyshkina, M. V., Nakamura, R., Baumjohann, W., Runov, A., ... Khotyaintsev, Y. (2007). Multi-spacecraft observation of plasma dipolarization/injection in the inner magnetosphere. *Annales Geophysicae*, *25*(3), 801–814. doi: 10.5194/angeo-25-801-2007

Artemyev, A. V., Liu, J., Angelopoulos, V., & Runov, A. (2015). Acceleration of ions by electric field pulses in the inner magnetosphere. *Journal of Geophysical Research: Space Physics*, *120*(6), 4628–4640. doi: 10.1002/2015JA021160

Artemyev, A. V., Lutsenko, V. N., & Petrukovich, A. A. (2012). Ion resonance acceleration by dipolarization fronts: analytic theory and spacecraft observation. *Annales Geophysicae*, *30*(2), 317–324. doi: 10.5194/angeo-30-317-2012

Baumjohann, W., Paschmann, G., & Lühr, H. (1990). Characteristics of high-speed ion flows in the plasma sheet. *Journal of Geophysical Research*, *95*(A4), 3801–3809. doi: 10.1029/JA095iA04p03801

Bingham, S. T., Cohen, I. J., Mauk, B. H., Turner, D. L., Mitchell, D. G., Vines, S. K., ... Burch, J. L. (2020). Charge-state-dependent energization of suprathermal ions during substorm injections observed by MMS in the magnetotail. *Journal of Geophysical Research: Space Physics*, *125*. doi: 10.1029/2020JA028144

Bingham, S. T., Nikoukar, R., Cohen, I. J., Mauk, B. H., Turner, D. L., Mitchell, D. G., ... Torbert, R. B. (2021). Evidence for nonadiabatic oxygen energization in the near-Earth magnetotail from MMS. *Geophysical Research Letters*, *48*. doi: 10.1029/2020GL091697

Birn, J., & Hesse, M. (1994). Particle acceleration in the dynamic magnetotail: Orbits in self-consistent three-dimensional MHD fields. *Journal of Geophysical Research*, *99*(A1), 109. doi: 10.1029/93JA02284

Birn, J., Hesse, M., Nakamura, R., & Zaharia, S. (2013). Particle acceleration in dipolarization events. *Journal of Geophysical Research: Space Physics*, *118*(5), 1960–1971. doi: 10.1002/jgra.50132

Birn, J., Runov, A., & Hesse, M. (2015). Energetic ions in dipolarization events. *Journal of Geophysical Research: Space Physics*, *120*(9), 7698–7717. doi: 10.1002/2015JA021372

Birn, J., Runov, A., & Zhou, X. (2017). Ion velocity distributions in dipolarization events: Distributions in the central plasma sheet. *Journal of Geophysical Research: Space Physics*, *122*(8), 8014–8025. doi: 10.1002/2017JA024230

Birn, J., Thomsen, M. F., Borovsky, J. E., Reeves, G. D., & Hesse, M. (2000). Particle acceleration in the dynamic magnetotail. *Physics of Plasmas*, *7*(5), 2149–2156. doi: 10.1063/1.874035

Birn, J., Thomsen, M. F., Borovsky, J. E., Reeves, G. D., McComas, D. J., Belian, R. D., & Hesse, M. (1997). Substorm ion injections: Geosynchronous observations and test particle orbits in three-dimensional dynamic MHD fields. *Journal of Geophysical Research: Space Physics*, *102*(A2), 2325–2341. doi: 10.1029/96JA03032

Blake, J. B., Mauk, B. H., Baker, D. N., Carranza, P., Clemmons, J. H., Craft, J., ... Westlake, J. (2016). The Fly's Eye Energetic Particle Spectrometer (FEEPS) Sensors for the Magnetospheric Multiscale (MMS) Mission. *Space Science Reviews*, *199*(1-4), 309–329. doi: 10.1007/s11214-015-0163-x

Catapano, F., Zimbardo, G., Perri, S., Greco, A., Delcourt, D., Retinò, A., & Cohen, I. J. (2017). Charge Proportional and Weakly Mass-Dependent Acceleration of Different Ion Species in the Earth's Magnetotail. *Geophysical Research Letters*, *44*, 10108–10115. doi: 10.1002/2017GL075092

Chen, C. X., & Wolf, R. A. (1999). Theory of thin-filament motion in Earth's magnetotail and its application to bursty bulk flows. *Journal of Geophysical Research: Space Physics*, *104*(A7), 14613–14626. doi: 10.1029/1999JA900005

Cohen, I. J., Mitchell, D. G., Kistler, L. M., Mauk, B. H., Anderson, B. J., Westlake, J. H., ... Burch, J. L. (2017). Dominance of high-energy (>150 keV) heavy ion intensities in Earth's middle to outer magnetosphere. *Journal of Geophysical Research: Space Physics*, *122*(9), 9282–9293. doi: 10.1002/2017JA024351

Ergun, R. E., Tucker, S., Westfall, J., Goodrich, K. A., Malaspina, D. M., Summers, D., ... Cully, C. M. (2016). The Axial Double Probe and Fields Signal Processing for the MMS Mission. *Space Science Reviews*, *199*(1-4), 167–188. doi: 10.1007/s11214-014-0115-x

Fu, H. S., Grigorenko, E. E., Gabrielse, C., Liu, C., Lu, S., Hwang, K. J., ... Chen, F. (2020). Magnetotail dipolarization fronts and particle acceleration: A review. *Science China Earth Sciences*, *63*(2), 235–256. doi: 10.1007/s11430-019-9551-y

Fu, H. S., Khotyaintsev, Y. V., André, M., & Vaivads, A. (2011). Fermi and betatron acceleration of suprathermal electrons behind dipolarization fronts. *Geophysical Research Letters*, *38*, L16104. doi: 10.1029/2011GL048528

Fu, H. S., Khotyaintsev, Y. V., Vaivads, A., Retinò, A., & André, M. (2013). Energetic electron acceleration by unsteady magnetic reconnection. *Nature Physics*, *9*(7), 426–430. doi: 10.1038/nphys2664

Gershman, D. J., Dorelli, J. C., Avanov, L. A., Gliese, U., Barrie, A., Schiff, C., ... Pollock, C. J. (2019). Systematic uncertainties in plasma parameters reported by the Fast Plasma Investigation on NASA's Magnetospheric Multiscale mission. *Journal of Geophysical Research: Space Physics*, *124*(12), 10345–10359. doi: 10.1029/2019JA026980

Gosling, J. T., Thomsen, M. F., Bame, S. J., Feldman, W. C., Paschmann, G., & Sckopke, N. (1982). Evidence for specularly reflected ions upstream from the quasi-parallel bow shock. *Geophysical Research Letters*, *9*(12), 1333–1336. doi: 10.1029/GL009i012p01333

Haaland, S., Kronberg, E. A., Daly, P. W., Fränz, M., Degener, L., Georgescu, E., & Dandouras, I. (2010). Spectral characteristics of protons in the Earth's plasmasheet: statistical results from Cluster CIS and RAPID. *Annales Geophysicae*, *28*(8), 1483–1498. doi: 10.5194/angeo-28-1483-2010

Keika, K., Kistler, L. M., & Brandt, P. (2013). Energization of O+ ions in the Earth's inner magnetosphere and the effects on ring current buildup: A review of previous observations and possible mechanisms. *Journal of Geophysical Research: Space Physics*, *118*(7), 4441–4464. doi: 10.1002/jgra.50371

Khotyaintsev, Y. V., Cully, C. M., Vaivads, A., André, M., & Owen, C. J. (2011). Plasma jet braking: Energy dissipation and nonadiabatic electrons. *Physical Review Letters*,

106(16), 165001. doi: 10.1103/PhysRevLett.106.165001

Kistler, L. M., Ipavich, F. M., Hamilton, D. C., Gloeckler, G., Wilken, B., Kremser, G., & Stüdemann, W. (1989). Energy spectra of the major ion species in the ring current during geomagnetic storms. *Journal of Geophysical Research*, *94*(A4), 3579–3599. doi: 10.1029/JA094iA04p03579

Lindqvist, P.-A., Olsson, G., Torbert, R. B., King, B., Granoff, M., Rau, D., ... Tucker, S. (2016). The Spin-Plane Double Probe Electric Field Instrument for MMS. *Space Science Reviews*, *199*(1-4), 137–165. doi: 10.1007/s11214-014-0116-9

Liu, J., Angelopoulos, V., Runov, A., & Zhou, X.-Z. (2013). On the current sheets surrounding dipolarizing flux bundles in the magnetotail: The case for wedgelets. *Journal of Geophysical Research: Space Physics*, *118*(5), 2000–2020. doi: 10.1002/jgra.50092

Malykhin, A. Y., Grigorenko, E. E., Kronberg, E. A., Koleva, R., Ganushkina, N. Y., Kozak, L., & Daly, P. W. (2018). Contrasting dynamics of electrons and protons in the near-Earth plasma sheet during dipolarization. *Annales Geophysicae*, *36*(3), 741–760. doi: 10.5194/angeo-36-741-2018

Masuda, S., Kosugi, T., Hara, H., Tsuneta, S., & Ogawara, Y. (1994). A loop-top hard X-ray source in a compact solar flare as evidence for magnetic reconnection. *Nature*, *371*(6497), 495–497. doi: 10.1038/371495a0

Mauk, B. H., Blake, J. B., Baker, D. N., Clemmons, J. H., Reeves, G. D., Spence, H. E., ... Westlake, J. H. (2016). The Energetic Particle Detector (EPD) Investigation and the Energetic Ion Spectrometer (EIS) for the Magnetospheric Multiscale (MMS) Mission. *Space Science Reviews*, *199*(1-4), 471–514. doi: 10.1007/s11214-014-0055-5

Merkin, V. G., Panov, E. V., Sorathia, K. A., & Ukhorskiy, A. Y. (2019). Contribution of bursty bulk flows to the global dipolarization of the magnetotail during an isolated substorm. *Journal of Geophysical Research: Space Physics*, *124*(11), 8647–8668. doi: 10.1029/2019JA026872

Mitchell, D. G., Gkioulidou, M., & Ukhorskiy, A. Y. (2018). Energetic ion injections inside geosynchronous orbit: Convection- and drift-dominated, charge-dependent adiabatic energization (W = qEd). *Journal of Geophysical Research: Space Physics*, *123*(8), 6360–6382. doi: 10.1029/2018JA025556

Nakamura, R., Baumjohann, W., Klecker, B., Bogdanova, Y., Balogh, A., Rème, H., ... Runov, A. (2002). Motion of the dipolarization front during a flow burst event observed by Cluster. *Geophysical Research Letters*, *29*(20), 1942. doi: 10.1029/2002GL015763

Nakamura, R., Baumjohann, W., Mouikis, C., Kistler, L. M., Runov, A., Volwerk, M., ... Balogh, A. (2004). Spatial scale of high-speed flows in the plasma sheet observed by Cluster. *Geophysical Research Letters*, *31*, L09804. doi: 10.1029/2004GL019558

Ohtani, S. (2004). Temporal structure of the fast convective flow in the plasma sheet: Comparison between observations and two-fluid simulations. *Journal of Geophysical Research*, *109*, A03210. doi: 10.1029/2003JA010002

Panov, E. V., Nakamura, R., Baumjohann, W., Angelopoulos, V., Petrukovich, A. A., Retinò, A., ... Larson, D. (2010). Multiple overshoot and rebound of a bursty bulk flow. *Geophysical Research Letters*, *37*(8). doi: 10.1029/2009GL041971

Phan, T. D., Kistler, L. M., Klecker, B., Haerendel, G., Paschmann, G., Sonnerup, B. U. Ö., ... Reme, H. (2000). Extended magnetic reconnection at the Earth's magnetopause from detection of bi-directional jets. *Nature*, *404*(6780), 848–850. doi: 10.1038/35009050

Pollock, C., Moore, T., Jacques, A., Burch, J., Gliese, U., Saito, Y., ... Zeuch, M. (2016). Fast Plasma Investigation for Magnetospheric Multiscale. *Space Science Reviews*, *199*(1-4), 331–406. doi: 10.1007/s11214-016-0245-4

Pritchett, P. L., & Coroniti, F. V. (2010). A kinetic ballooning/interchange instability in the magnetotail. *Journal of Geophysical Research: Space Physics*, *115*(A06301). doi: 10.1029/2009JA014752

Pudritz, R. E., Hardcastle, M. J., & Gabuzda, D. C. (2012). Magnetic fields in astrophysical jets: From launch to termination. *Space Science Reviews*, *169*(1-4), 27–72. doi: 10.1007/s11214-012-9895-z

Runov, A., Angelopoulos, V., Gabrielse, C., Liu, J., Turner, D. L., & Zhou, X. (2015). Average thermodynamic and spectral properties of plasma in and around dipolarizing flux bundles. *Journal of Geophysical Research: Space Physics*, *120*(6), 4369–4383. doi: 10.1002/2015JA021166

Runov, A., Angelopoulos, V., Sitnov, M. I., Sergeev, V. A., Bonnell, J., McFadden, J. P., ... Auster, U. (2009). THEMIS observations of an earthward-propagating dipolarization front. *Geophysical Research Letters*, *36*, L14106. doi: 10.1029/2009GL038980

Runov, A., Angelopoulos, V., Zhou, X.-Z., Zhang, X.-J., Li, S., Plaschke, F., & Bonnell, J. (2011). A THEMIS multicase study of dipolarization fronts in the magnetotail plasma sheet. *Journal of Geophysical Research: Space Physics*, *116*, A05216. doi: 10.1029/2010JA016316

Russell, C. T., Anderson, B. J., Baumjohann, W., Bromund, K. R., Dearborn, D., Fischer, D., ... Richter, I. (2016). The Magnetospheric Multiscale Magnetometers. *Space Science Reviews*, *199*(1-4), 189–256. doi: 10.1007/s11214-014-0057-3

Schulz, M., & Lanzerotti, L. J. (1974). *Particle Diffusion in the Radiation Belts* (Vol. 7; J. G. Roederer, Ed.). Berlin, Heidelberg: Springer Berlin Heidelberg. doi: 10.1007/978-3-642-65675-0

Sergeev, V., Angelopoulos, V., Apatenkov, S., Bonnell, J., Ergun, R., Nakamura, R., ... Runov, A. (2009). Kinetic structure of the sharp injection/dipolarization front in the flow-braking region. *Geophysical Research Letters*, *36*(L21105). doi: 10.1029/2009GL040658

Sitnov, M. I., Birn, J., Ferdousi, B., Gordeev, E., Khotyaintsev, Y. V., Merkin, V. G., ... Zhou, X. (2019). Explosive magnetotail activity. *Space Science Reviews*, *215*(4), 31. doi: 10.1007/s11214-019-0599-5

Sitnov, M. I., Swisdak, M., & Divin, A. V. (2009). Dipolarization fronts as a signature of transient reconnection in the magnetotail. *Journal of Geophysical Research: Space Physics*, *114*(A04202). doi: 10.1029/2008JA013980

Tsyganenko, N. (1989). A magnetospheric magnetic field model with a warped tail current sheet. *Planetary and Space Science*, *37*(1), 5–20. doi: 10.1016/0032-0633(89)90066-4

Turner, D. L., Fennell, J. F., Blake, J. B., Clemmons, J. H., Mauk, B. H., Cohen, I. J., ... Burch, J. L. (2016). Energy limits of electron acceleration in the plasma sheet during substorms: A case study with the Magnetospheric Multiscale (MMS) mission. *Geophysical Research Letters*, *43*, 7785–7794. doi: 10.1002/2016GL069691

Ukhorskiy, A. Y., Sitnov, M. I., Merkin, V. G., & Artemyev, A. V. (2013). Rapid acceleration of protons upstream of earthward propagating dipolarization fronts. *Journal of Geophysical Research: Space Physics*, *118*(8), 4952–4962. doi: 10.1002/jgra.50452

Ukhorskiy, A. Y., Sitnov, M. I., Merkin, V. G., Gkioulidou, M., & Mitchell, D. G. (2017). Ion acceleration at dipolarization fronts in the inner magnetosphere. *Journal of Geophysical Research: Space Physics*, *122*(3), 3040–3054. doi: 10.1002/2016JA023304

Ukhorskiy, A. Y., Sorathia, K. A., Merkin, V. G., Sitnov, M. I., Mitchell, D. G., & Gkioulidou, M. (2018). Ion trapping and acceleration at dipolarization fronts: High-resolution MHD and test-particle simulations. *Journal of Geophysical Research: Space Physics*, *123*(7), 5580–5589. doi: 10.1029/2018JA025370

Young, D. T., Burch, J. L., Gomez, R. G., De Los Santos, A., Miller, G. P., Wilson, P., ... Webster, J. M. (2016). Hot Plasma Composition Analyzer for the Magnetospheric Multiscale Mission. *Space Science Reviews*, *199*(1-4), 407–470. doi: 10.1007/s11214-014-0119-6

Zhou, X.-Z., Angelopoulos, V., Sergeev, V. A., & Runov, A. (2010). Accelerated ions ahead of earthward propagating dipolarization fronts. *Journal of Geophysical Research: Space Physics*, *115*(A00I03). doi: 10.1029/2010JA015481

Zhou, X.-Z., Angelopoulos, V., Sergeev, V. A., & Runov, A. (2011). On the nature of precursor flows upstream of advancing dipolarization fronts. *Journal of Geophysical Research: Space Physics*, *116*(A03222). doi: 10.1029/2010JA016165

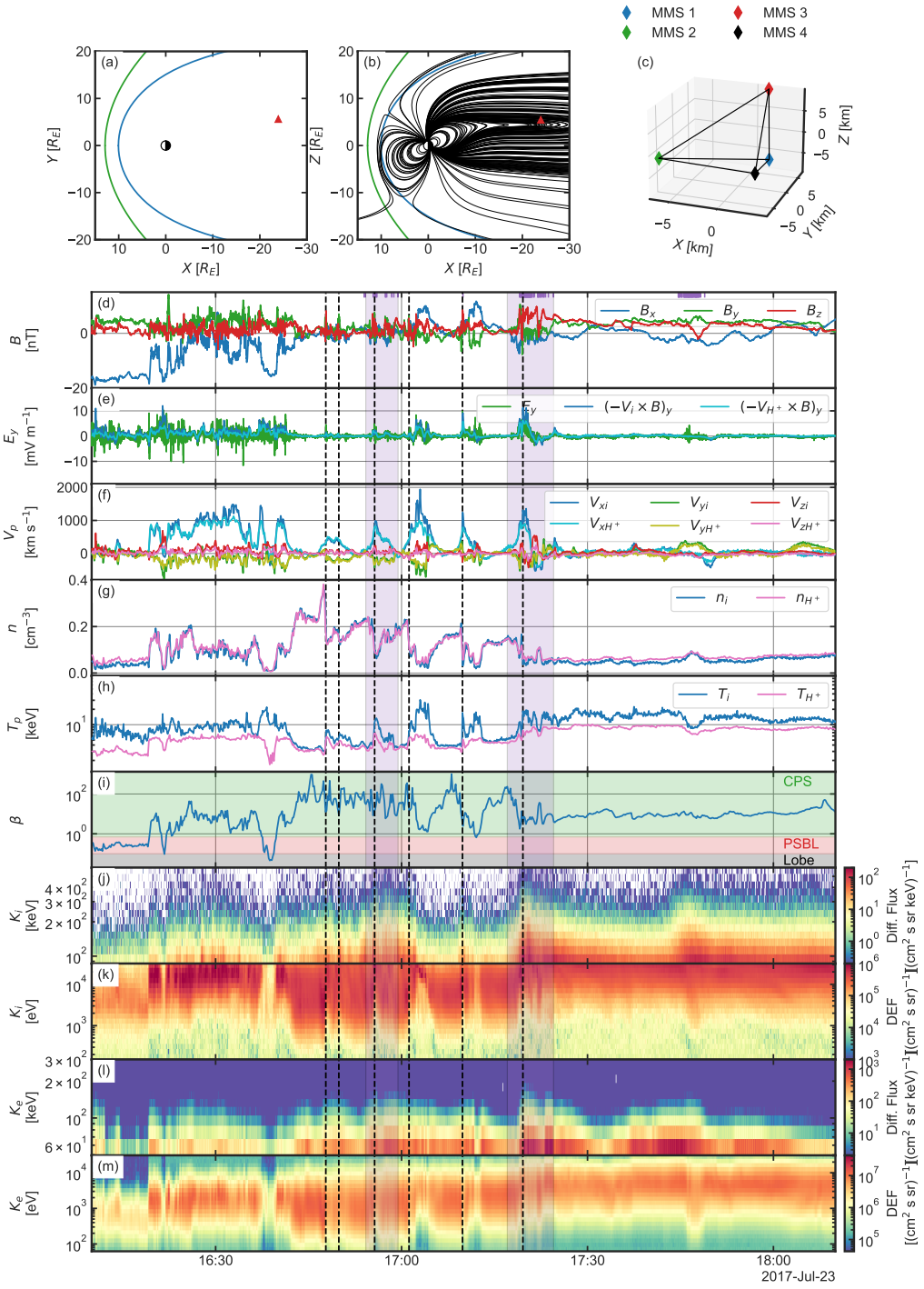

Figure 1. Overview of the event. (a)-(b) Location of the MMS spacecraft in GSE coordinates with the earth's bow shock (green), the earth's magnetopause (blue) and the magnetic field lines computed using the T89 model (black). (c) MMS tetrahedron configuration. (d) Magnetic field in GSM coordinates. (e) Dawn-dusk (GSM) electric field. (f) Proton bulk velocity in GSM coordinates. (g) Proton (blue and cyan) and alpha particles (green) number density. (h) Proton temperature. (i) Plasma parameter β. (j) Omni-directional ion differential particle flux. (k) Omni-directional ion differential energy flux. (l) Omni-directional electron differential particle flux. (m) Omni-directional electron differential energy flux. The purple dots in panel (d) are the energization times defined in Equation 1. The black dashed lines indicate the peaks in the energetic ion flux (panel (j)).

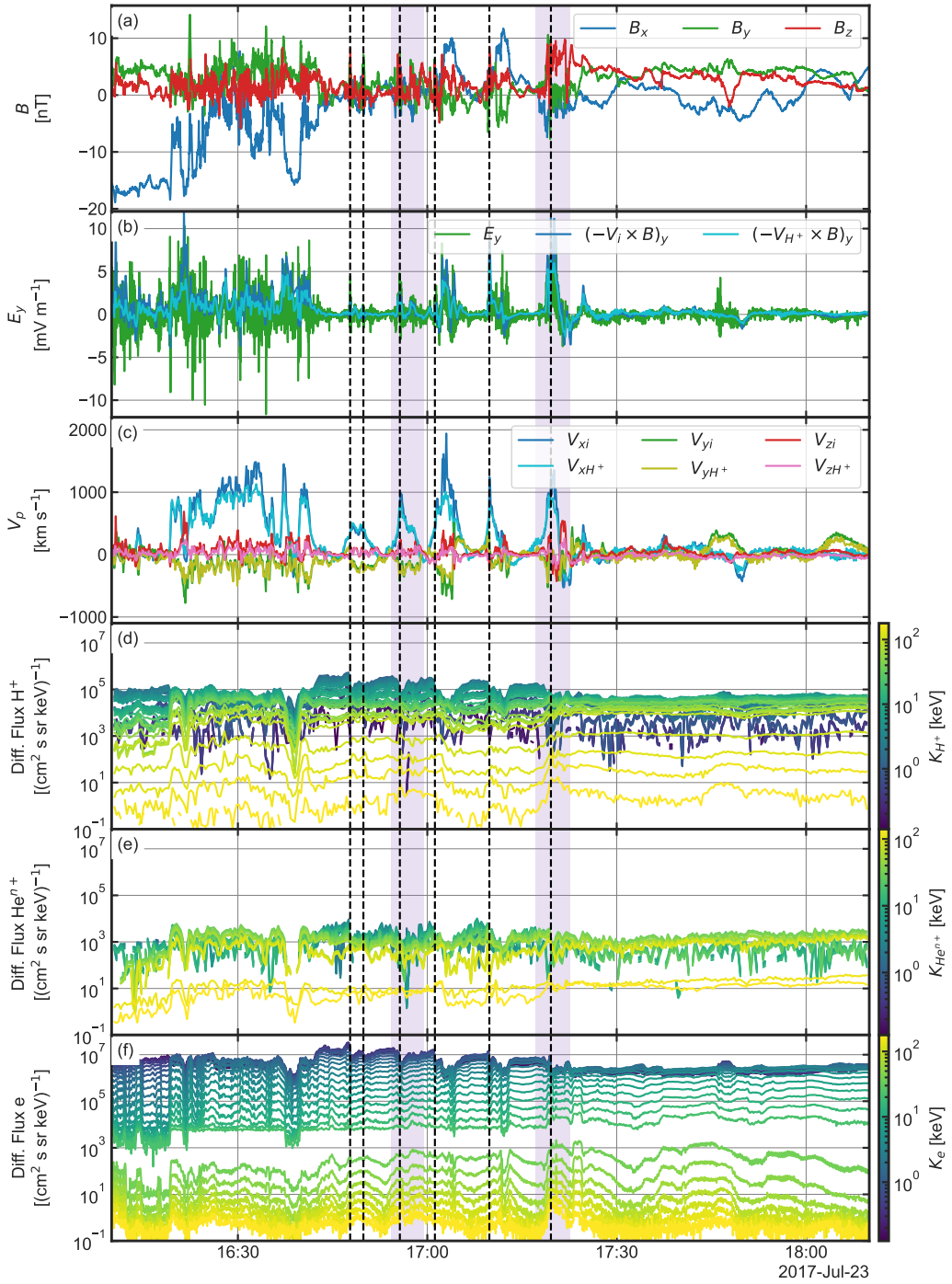

Figure 2. Ion (H^+ and He^{n+}) and electron flux changes. (a) Magnetic field in GSM coordinates. (b) Dawn-dusk cross-tail electric field from EDP (green), FPI-DIS $\mathbf{V_i}\times\mathbf{B}$ (blue) and HPCA $\mathbf{V_{H^+}}\times\mathbf{B}$ (cyan). (c) Ion bulk velocity from FPI-DIS and HPCA. (d) H^+ flux time series from combined FPI-DIS and EIS. (e) He^{n+} flux time series from combined HPCA and EIS. (f) Electron flux time series from combined FPI-DES and EIS. The black dashed lines indicate the injections.

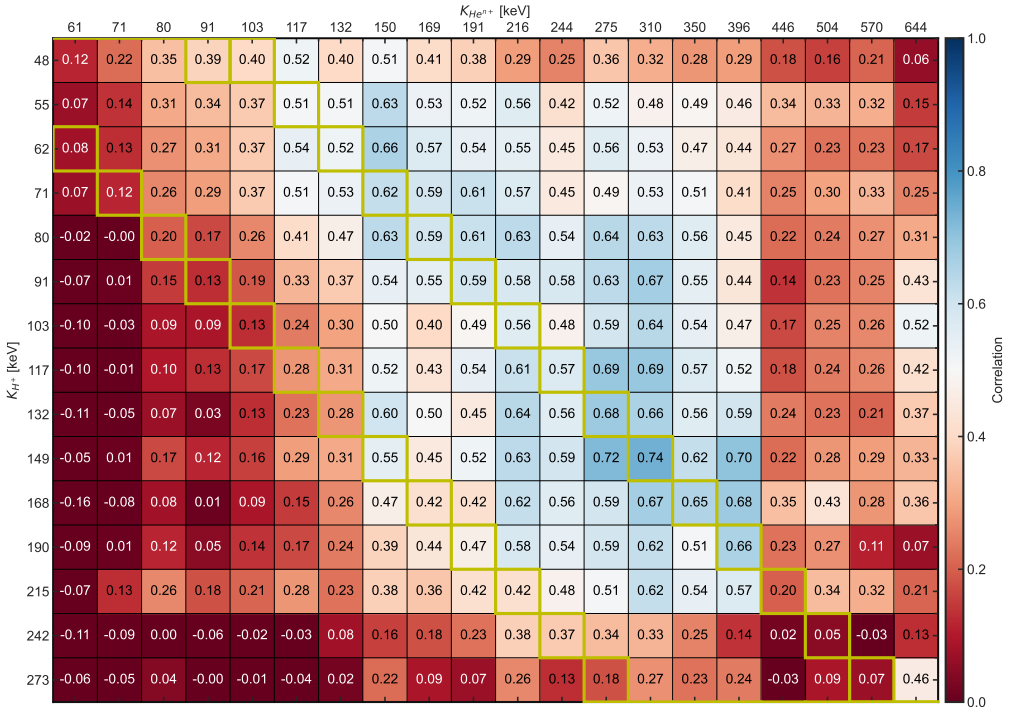

Figure 3. Cross-correlation coefficients between the time series of H^+ and He^{n+} from EIS measurements at different energies taken between 16:10-18:10 UT on July 23, 2017. The yellow boxes indicate $K_{He^{n+}} = 1 * K_{H^+}$ (lower left diagonal) and $K_{He^{n+}} = 2 * K_{H^+}$ (upper right diagonal)

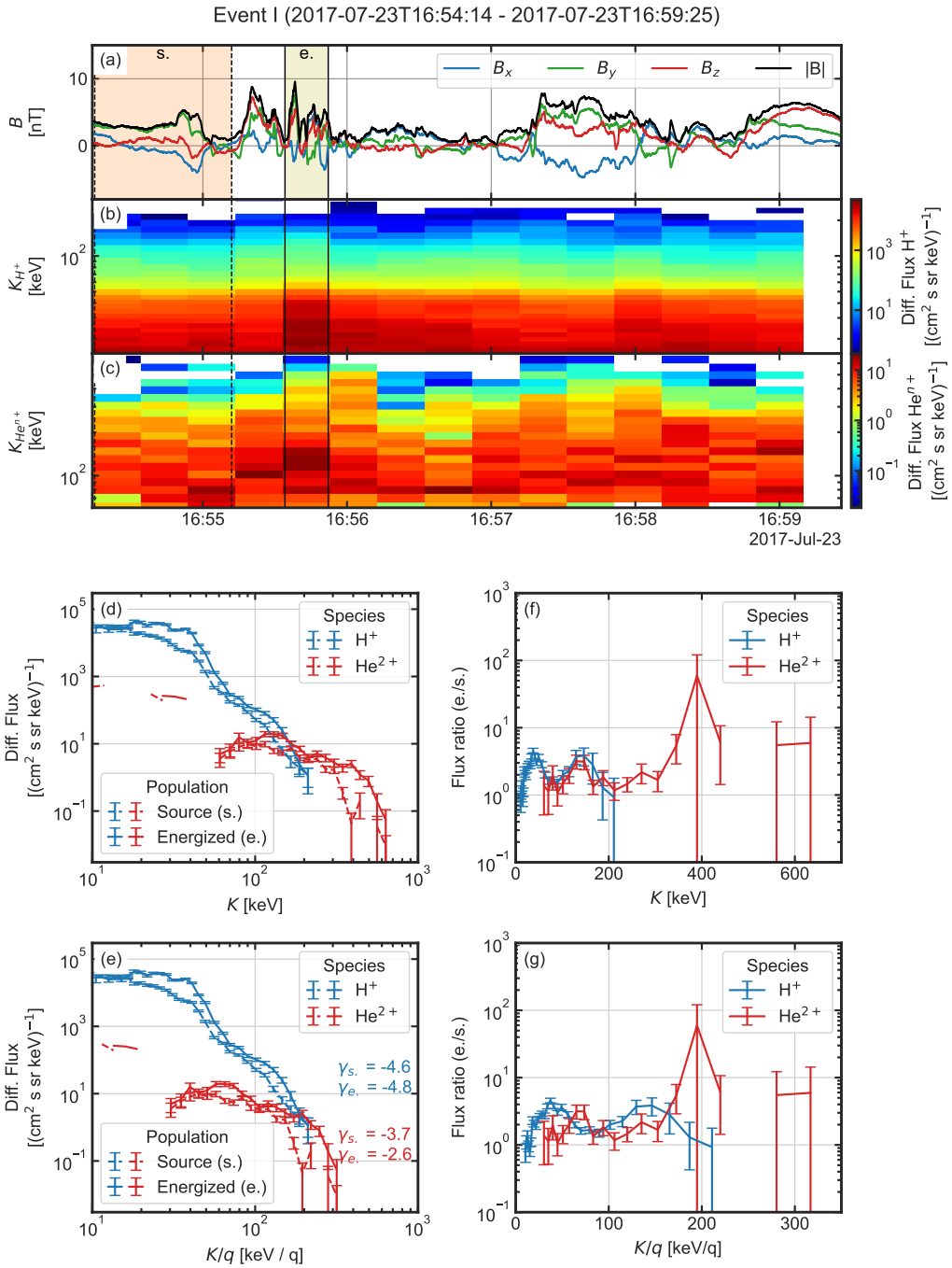

Figure 4. H^+ and He^{n+} source and energized flux spectra for event I. (a) Magnetic field in GSM coordinates. (b) EIS H^+ omni-directional flux energy spectrum. (c) EIS He^{n+} omni-directional flux energy spectrum. H^+ (blue) and He^{n+} (red) flux energy spectra in the source (dashed line) and energized (solid line) regions as a function of the energy K (d) and the energy per charge K/q (e). H^+ (blue) and He^{n+} (red) energized to source flux ratio energy spectra as a function of the energy K (f) and the energy per charge K/q (g).

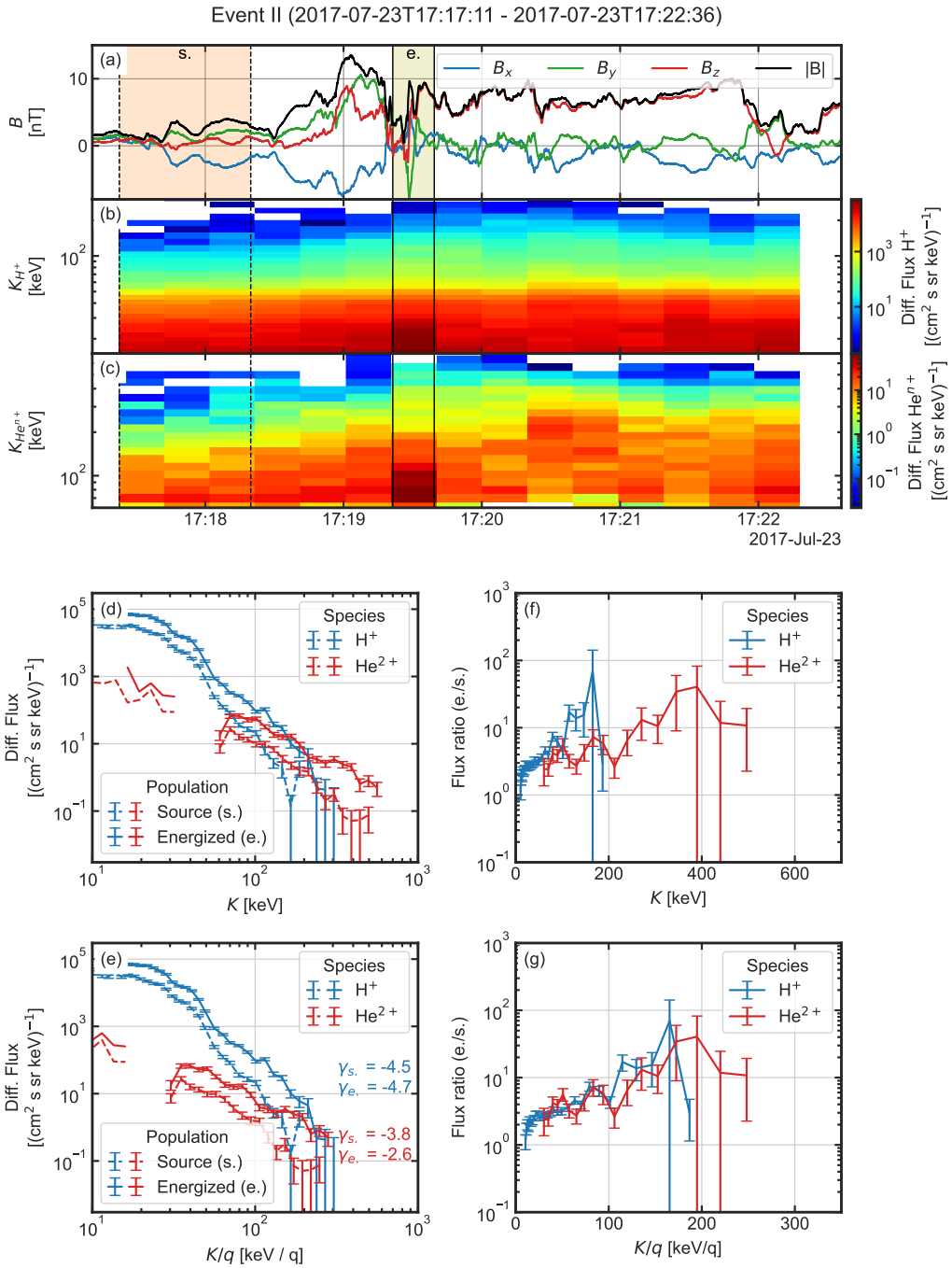

Figure 5. H^+ and He^{n+} source and energized flux spectra for event II. (a) Magnetic field in GSM coordinates. (b) EIS H^+ omni-directional flux energy spectrum. (c) EIS He^{n+} omni-directional flux energy spectrum. H^+ (blue) and He^{n+} (red) flux energy spectra in the source (dashed line) and energized (solid line) regions as a function of the energy K (d) and the energy per charge K/q (e). H^+ (blue) and He^{n+} (red) energized to source flux ratio energy spectra as a function of the energy K (f) and the energy per charge K/q (g).

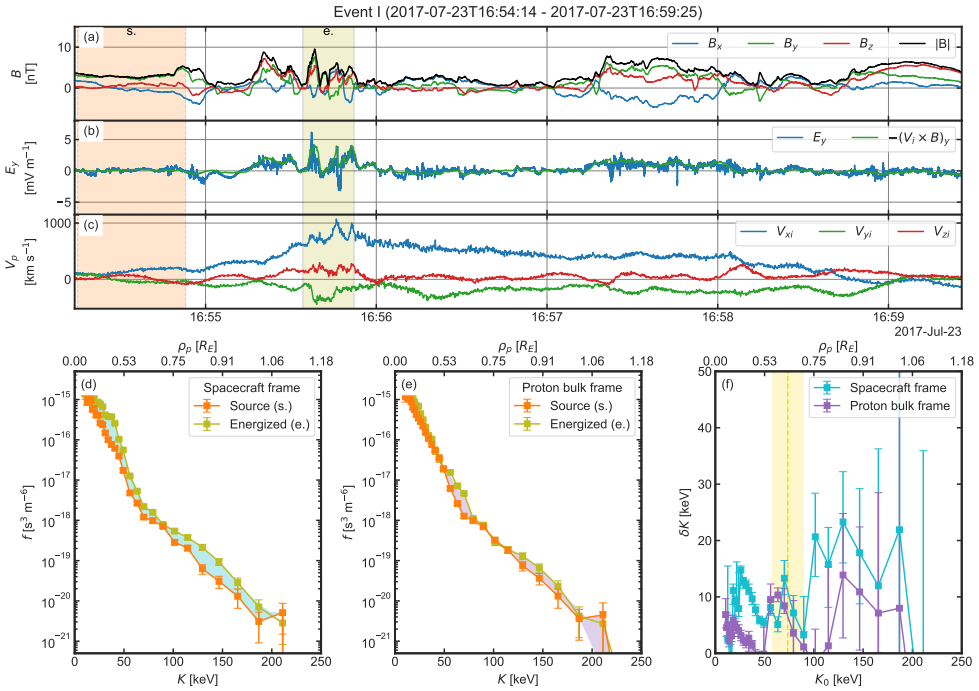

Figure 6. Proton flux energy spectrum in the spacecraft and proton frame for event I. (a) Magnetic field in GSM coordinates. (b) Dawn-dusk cross-tail electric field from EDP (blue) and $-V_i \times B$ (green). (c) Ion bulk velocity in GSM coordinates. The orange and green shaded regions in panels (a)-(c) show the source and energized regions. (d) Source (orange) and energized (green) proton phase space density energy spectrum in the spacecraft frame. The cyan area emphasize the difference between the two lines. (e) Source (orange) and energized (green) proton phase space density energy spectrum in the proton bulk frame. The purple area emphasize the difference between the two lines. (f) Energy increase in the spacecraft frame (cyan) and proton bulk frame (purple). The gold line shows the energy of a proton with a gyroradius of $\rho_p = L_{pulse}$ (see text).

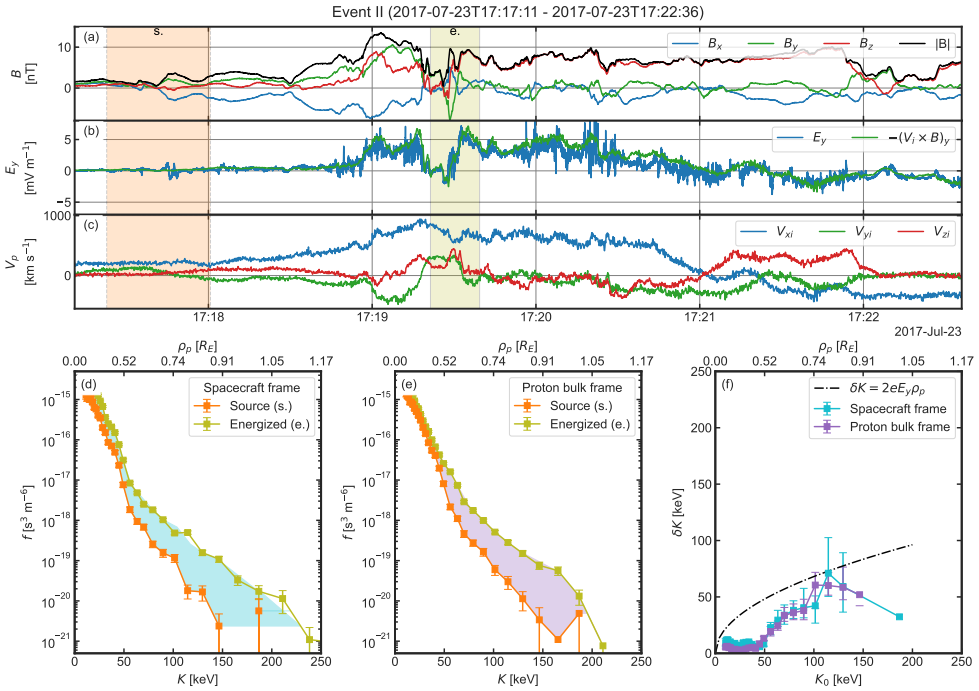

Figure 7. Proton flux energy spectrum in the spacecraft and proton frame for event II. (a) Magnetic field in GSM coordinates. (b) Dawn-dusk cross-tail electric field from EDP (blue) and $-V_i \times B$ (green). (c) Ion bulk velocity in GSM coordinates. The orange and green shaded regions in panels (a)-(c) show the source and energized regions. (d) Source (orange) and energized (green) proton phase space density energy spectrum in the spacecraft frame. The cyan area emphasize the difference between the two lines. (e) Source (orange) and energized (green) proton phase space density energy spectrum in the proton bulk frame. The purple area emphasize the difference between the two lines. (f) Energy increase in the spacecraft frame (cyan) and proton bulk frame (purple). The black dash-dotted line shows the model $\delta K = 2eE_y\rho_p$.